

Research Article

Adaptive Extended Kalman Filter and Point-Ahead Angle Prediction in the Detection of Gravitational Waves in Space

Jianjun Jia¹, Yun Kau Lau²

1. Independent researcher; 2. Institute of Applied Mathematics, Morningside Center of Mathematics, LSSC, Chinese Academy of Sciences, Beijing, China

In the detection of gravitational waves in space, during the science phase of the mission, the point ahead angle mechanism (PAAM) serves to steer a laser beam to compensate for the angle generated by the relative motion of the two spacecrafts (SCs) during the approximately 10 seconds of flight time a laser beam will take from one SC to reach a distant SC of three million kilometers away. The common practice for pointing stability control of a laser beam is to first do a coarse tracking by the PAAM to steer a laser beam to compensate for the relative motion between two SCs, to be followed by a fine pointing stability control. In the present work, by exploiting the near-circular orbit structure of individual SC in the triangular constellation, the feasibility of inserting an adaptive Kalman filter (AEKF) into the PAAM control loop is investigated. By adopting a colored measurement noise model that closely resembles the prospective on orbit situation, numerical simulation suggests that the dynamic range of the PAAM may be reduced to the level of nano-radians using the prediction of the pointing head angle (PAA) by the AEKF. This will cut down on the TTL coupling noise and the position noise budget allocated to the PAAM. This in turn reduces the dynamic range of the fine pointing control and leaves room to improve its accuracy, thereby offers the prospect of reduction of the position noise budget allocated to the laser pointing instability as a whole.

Corresponding authors: Jianjun Jia, jjun10@mail.sitp.ac.cn; Yun Kau Lau, lau@amss.ac.cn

I. Introduction

In detecting gravitational waves in space, the PAAM serves different functions at different stages of the mission. During the scientific phase of a mission, due to the million kilometers apart between two SCs, a

laser beam emanating from one SC will take about ten seconds to reach a distant one. Between this time interval, the distant SC moves, and the PAAM serves to steer a laser beam to compensate for the distance traversed during this interval. At the same time, it also serves to compensate for the breathing angle generated by solar gravity at the annual level.

In the present work, we shall address problems related to the laser pointing control in relation to the PAAM stability during the scientific phase. We will confine our attention to the triangular constellation with heliocentric orbit^{[1][2]}. It is conceivable that the analysis may be applicable to triangular constellation in near earth orbit as well^[3]. The conventional practice for pointing stability control of an inter-satellite link is partitioned into two stages. The PAAM performs coarse pointing, to be followed in the second stage by a more accurate fine pointing control to achieve the accuracy of nano-radian pointing. The micro-radian angular jitter together with the piston noise of PAAM, when coupled with the position noise of the steering mechanism and the phase center offset from the center of mass of a SC, will generate position noise for the gravitational wave measurement.

Given the simple near-circular orbit of each SC in the triangular satellite formation in the detection of gravitational waves in space, it is natural to inquire whether an AEKF based on the orbital dynamics may be incorporated into the PAAM control loop so that the pointing accuracy may be improved and the dynamic range of the PAAM is reduced at the same time. This will cut down on the position noise budget for the PAAM and mitigate at least partially the TTL noise generated by the PAAM. As a preliminary step to explore this line of thought, the aim of the present work is to study this problem more in-depth by means of simulation. The work to be presented in what follows suggests that AEKF does have the potential to play an instrumental role in the PAAM control loop.

The structure of this paper is organized as follows. Some background materials concerning PAA and AEKF with colored noise are introduced in sections 2 and 3, respectively. Section 4 presents the design of the control loop for the PAAM with the insertion of AEKF. We begin to enter the core of our work in section 5 and set up the AEKF framework for the PAAM. The system noise model to be employed in the AEKF is worked out in section 6. Section 7 discusses the measurement noise model in the AEKF and the generation of random time-domain noise signals with prescribed PSD used in the simulation. Section 8 presents the simulation results and conducts an in-depth analysis of the filtering results obtained from AEKF. In the final section, some remarks that look to the future of this work are made to conclude our work.

II. PAAM—some basics

In this section, we shall review some basics of the PAAM. This serves to provide background for subsequent discussions and at the same time fix notations and conventions.

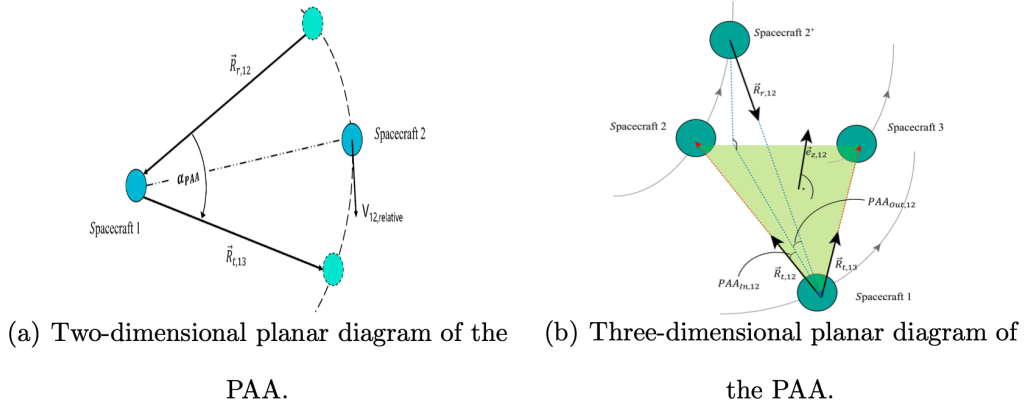


Figure 1. Definition of in-Plane and out-of-Plane PAAs

PAA is the angle formed between the direction of the transmitted beam between the local SC and the remote SC and the direction of the received beam between the remote SC and the local SC, as shown in Fig. 1. The angle varies annually with the orbit of the triangular constellation. Throughout this work, we shall adopt the J2000.0 coordinate system to describe the position and velocity of SCs. The J2000.0 coordinate system is based on the North Celestial Pole and the Vernal Equinox of epoch J2000.0, with the Z axis pointing to the North Celestial Pole, the X axis pointing to the Vernal Equinox, and the X, Y, and Z axes forming a right-handed rectangular coordinate system. The positions and velocities of SCi (i=1,2,3) at a certain epoch may be expressed respectively as $[X_i, Y_i, Z_i]^T$, and $[V_{Xi}, V_{Yi}, V_{Zi}]^T$. The relative position and velocity of two SCs are then given by vector addition or subtraction with respect to the J2000.0 reference frame.

II.1. Calculations of PAA

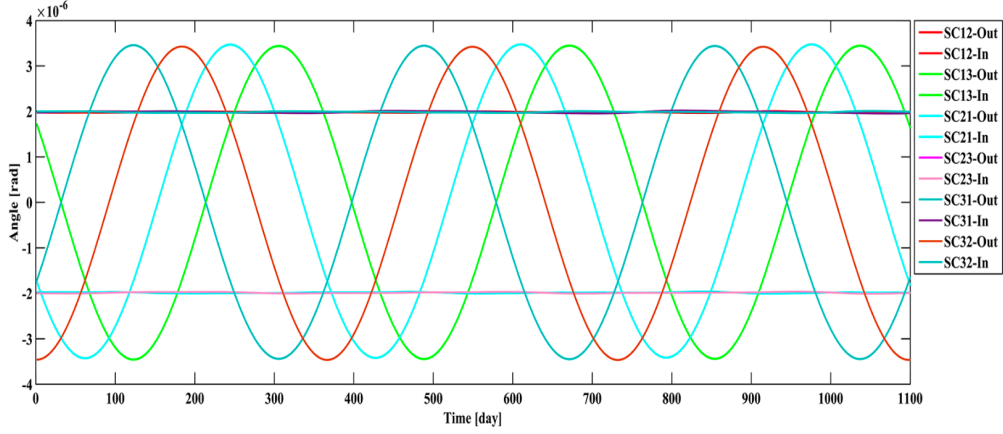


Figure 2. Dynamic range of PAAs.

Fig. 1 illustrates the in-plane and out-of-plane PAAs. Fig. 2 displays the dynamic range of PAAs. Denote by $\vec{R}_{t,ij}$ $i, j = 1, 2, 3$ the beam vector linking a local SC to a remote SC. $\vec{R}_{r,ij}$ is the beam vector linking remote SC to the local SC. The PAA may be calculated to be

$$\text{PAA} = \arcsin \left| \frac{\vec{R}_{t,ij}}{|\vec{R}_{t,ij}|} \times \frac{\vec{R}_{r,ij}}{|\vec{R}_{r,ij}|} \right|. \quad (1)$$

Take $(i, j) = (1, 2)$ as example, $\Delta t_{r,12}$ is the time taken for a laser beam originating from SC1 to reach SC2 and $\Delta t_{t,12}$ is the time taken for a laser beam from SC2 to reach SC1 upon receiving the laser beam from SC1. We have

$$R_{r,12} = \left| \vec{R}_{12} - \Delta t_{r,12} \cdot \vec{V}_{12} \right| = c \Delta t_{r,12}, \quad (2)$$

$$R_{t,12} = \left| \vec{R}_{12} + \Delta t_{t,12} \cdot \vec{V}_{12} \right| = c \Delta t_{t,12}, \quad (3)$$

Numerical calculations with our orbit integrator enable us to infer that the variation in light time propagation between two SCs is 10 ± 0.013 seconds in one year, and the resulting change in PAA angle may be neglected^[4]. Therefore, we will adopt the approximation that $\Delta t_{r,12} = \Delta t_{t,12} = \Delta t \approx 10$ seconds in the calculations that follow.

We shall divide the PAA into two parts in the calculations: in-plane and out-of-plane, as shown in Fig. 1.

Define

$$\vec{e}_{x,12} = \frac{\vec{R}_{t,12}}{|\vec{R}_{t,12}|}, \quad (4)$$

$$\vec{e}_{z,12} = \frac{\vec{R}_{t,12} \times \vec{R}_{t,13}}{|\vec{R}_{t,12} \times \vec{R}_{t,13}|}, \quad (5)$$

$$\vec{e}_{y,12} = \vec{e}_{z,12} \times \vec{e}_{x,12}, \quad (6)$$

Which are the unit direction vectors pointing along the X, Z, and Y axes, respectively.

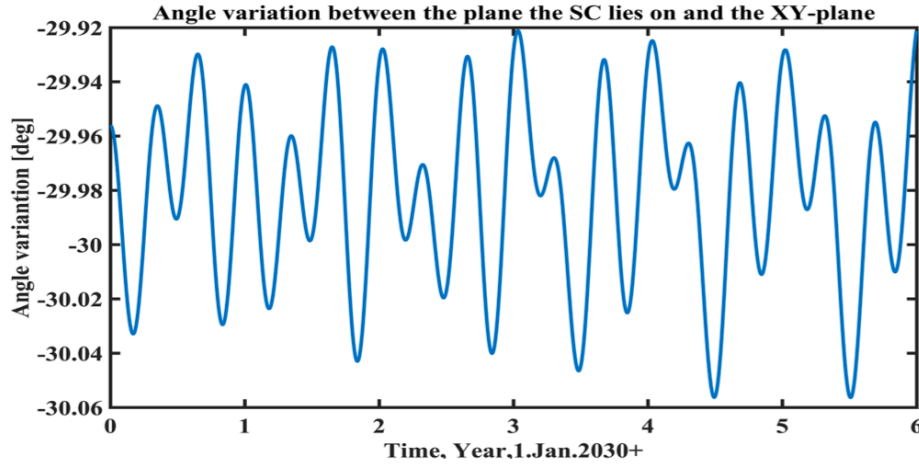


Figure 3. The angle variation between the constellation plane and the Heliocentric Ecliptic Coordinate System of J2000.0.

Fig. 3 shows the variation of the inclination angle between the triangle constellation plane and the ecliptic plane, with an annual variation range of around 0.08 degrees^[4]. This prompts us to approximate $\vec{e}_{z,12}$ as a constant vector. The error of the in-plane and out-of-plane PAAs due to this approximation is around 0.45 nrad, which is negligible compared to the half-angle of the beam ($\approx 1.43 \mu\text{rad}$)^[5].

The in-plane PAA is then given by

$$\text{PAA}_{\text{in},12} = \sin^{-1} \left(\frac{\vec{R}_{r,12} \times \vec{e}_{z,12}}{|\vec{R}_{r,12} \times \vec{e}_{z,12}|} \cdot \vec{e}_{x,12} \right) \approx \frac{\vec{R}_{r,12} \times \vec{e}_{z,12}}{|\vec{R}_{r,12} \times \vec{e}_{z,12}|} \cdot \vec{e}_{x,12}. \quad (7)$$

The out-of-plane PAA may be expressed as

$$\text{PAA}_{\text{out},12} = \sin^{-1} \left(\frac{\vec{e}_{z,12} \cdot \vec{R}_{r,12}}{|\vec{R}_{r,12}|} \right) \approx \frac{\vec{e}_{z,12} \cdot \vec{R}_{r,12}}{|\vec{R}_{r,12}|}. \quad (8)$$

In Eq. (7) and Eq. (8), we have used the approximation that $\sin x \approx x$, given that both $\text{PAA}_{\text{out},12}$ and $\text{PAA}_{\text{out},12}$ are of the order of μrad .

In the next step, we shall express the relative position and velocity vector between SCs in terms of the coordinate components in the J2000.0 frame. Let

$$\vec{R}_{12} = [x_{12}, y_{12}, z_{12}] = [X_1 - X_2, Y_1 - Y_2, Z_1 - Z_2], \quad (9)$$

represent the laser link directed from SC1 to SC2. Likewise,

$$\vec{V}_{12} = [V_{x12}, V_{y12}, V_{z12}] = [V_{X1} - V_{X2}, V_{Y1} - V_{Y2}, V_{Z1} - V_{Z2}], \quad (10)$$

is the relative velocity vector from SC1 to SC2. $[X_i, Y_i, Z_i]$ is the current position information of SCi with $i = 1, 2, 3$, and $[V_{Xi}, V_{Yi}, V_{Zi}]$ is the current velocity information of SCi. The beam vector $\vec{R}_{t,12}$ and beam vector $\vec{R}_{r,12}$ linking SC1 to SC2 may be expressed as

$$\vec{R}_{t,12} = [x_{12} + V_{x12} \Delta t, y_{12} + V_{y12} \Delta t, z_{12} + V_{z12} \Delta t], \quad (11)$$

$$\vec{R}_{r,12} = [x_{12} - V_{x12} \Delta t, y_{12} - V_{y12} \Delta t, z_{12} - V_{z12} \Delta t]. \quad (12)$$

The beam vector $\vec{R}_{t,13}$ linking SC1 to SC3 may be expressed as

$$\vec{R}_{t,13} = [x_{13} + V_{x13} \Delta t, y_{13} + V_{y13} \Delta t, z_{13} + V_{z13} \Delta t]. \quad (13)$$

According to Eq. (4)-Eq. (6), the X-axis directional vector of the SC1 may be expressed as

$$\vec{e}_{x,12} = \frac{[x_{12} + V_{x12} \Delta t, y_{12} + V_{y12} \Delta t, z_{12} + V_{z12} \Delta t]}{|\vec{R}_{t,12}|}. \quad (14)$$

Write $\vec{e}_{z,12}$ in terms of the coordinate components of J2000.0 as

$$\vec{e}_{z,12} = [e_{zx}, e_{zy}, e_{zz}]. \quad (15)$$

The Y-axis direction vector of SC1 may also be expressed in terms of the coordinate components of J2000.0 as

$$\vec{e}_{y,12} = \frac{1}{|\vec{R}_{t,12}|} \begin{bmatrix} (z_{12} + V_{z12} \Delta t)e_{zy} - (z_{12} + V_{z12} \Delta t)e_{zz} \\ (x_{12} + V_{x12} \Delta t)e_{zz} - (z_{12} + V_{z12} \Delta t)e_{zx} \\ (y_{12} + V_{y12} \Delta t)e_{zx} - (x_{12} + V_{x12} \Delta t)e_{zy} \end{bmatrix}^T. \quad (16)$$

Then the expression of in-plane PAA is given by

$$\text{PAA}_{\text{in},12} = \frac{\vec{R}_{r,12} \times \vec{e}_{z,12}}{|\vec{R}_{r,12} \times \vec{e}_{z,12}|} \cdot \vec{e}_{x,12} = \frac{(\vec{R}_{r,12} \times \vec{e}_{z,12}) \cdot \vec{e}_{x,12}}{|\vec{R}_{r,12}| |\vec{e}_{z,12}|}. \quad (17)$$

with

$$\begin{aligned}
(\vec{R}_{r,12} \times \vec{e}_{z,12}) \cdot \vec{e}_{x,12} = & ((y_{12} - V_{y_{12}} \Delta t) e_{zz} - (z_{12} - V_{z_{12}} \Delta t) e_{zy}) (x_{12} + V_{x_{12}} \Delta t) \\
& + ((z_{12} - V_{z_{12}} \Delta t) e_{zx} - (x_{12} - V_{x_{12}} \Delta t) e_{zz}) (y_{12} + V_{y_{12}} \Delta t) \\
& + ((x_{12} - V_{x_{12}} \Delta t) e_{zy} - (y_{12} - V_{y_{12}} \Delta t) e_{zx}) (z_{12} + V_{z_{12}} \Delta t).
\end{aligned} \tag{18}$$

The out-of-plane PAA is expressed as

$$\text{PAA}_{\text{out},12} = \frac{\vec{e}_{z,12} \cdot \vec{R}_{r,12}}{|\vec{R}_{r,12}|}. \tag{19}$$

with

$$\begin{aligned}
\vec{e}_{z,12} \cdot \vec{R}_{r,12} = & e_{zx} (x_{12} - V_{x_{12}} \Delta t) + e_{zy} (y_{12} - V_{y_{12}} \Delta t) \\
& + e_{zz} (z_{12} - V_{z_{12}} \Delta t).
\end{aligned} \tag{20}$$

III. Adaptive extended Kalman Filter

In this section, we shall introduce the AEKF method, on the basis of which we develop a new control algorithm for the PAAM. The material presented in this section is not new^[6], but to render the present article self-contained, we will describe the AEKF framework and then apply it to the PAAM in the next section.

Based on the standard EKF^{[7][6]}, we can treat the measurement noise as a state quantity and include it in the state equation^{[8][9]}. The state equation of the Kalman filter, which includes the extended system noise and the measurement noise, is obtained as Eq. (21).

$$\begin{bmatrix} X_{k+1} \\ v_{k+1} \end{bmatrix} = \begin{bmatrix} \phi_{k,k-1} & 0 \\ 0 & \Psi_{k,k-1} \end{bmatrix} \begin{bmatrix} X_k \\ v_k \end{bmatrix} + \begin{bmatrix} \Gamma_{k+1,k} & 0 \\ 0 & I \end{bmatrix} \begin{bmatrix} W_k \\ \xi_k \end{bmatrix}. \tag{21}$$

Where $\Gamma_{k+1,k}$ is an identity matrix. Based on the original measurement equation(?), make

$$Z_k^* = Z_{k+1} - \Psi_{k,k-1} \times Z_{k+1}. \tag{22}$$

It is obtained by substituting the expression Z_k

$$Z_{k+1} - \Psi_{k,k-1} Z_k = (H_{k+1} \phi_{k+1,k} - \Psi_{k,k-1} H_k) X_k + H_{k+1} \Gamma_k W_k + \xi_k. \tag{23}$$

We define $(H_{k+1} \phi_{k+1,k} - \Psi_{k,k-1} H_k)$ as H_k^* . $(H_{k+1} \Gamma_k W_k + \xi_k)$ is defined as V_k^* . Thus, a new measurement equation is established.

$$Z_k^* = H_k^* X_k + V_k^*, \tag{24}$$

Where V_k^* is zero mean white noise and its variance is

$$R_k^* = H_{k+1} \Gamma_k Q_k \Gamma_k^T H_{k+1}^T + R_k. \tag{25}$$

In this case, the covariance matrix of the measurement noise and the process noise is

$$S_k = Q_k \Gamma_k^T H_{k+1}^T + \xi_k. \quad (26)$$

The expression for the posterior estimation equation is

$$\hat{X}_{k+1} = \phi_{k+1,k} \hat{X}_k + \bar{K}_{k+1} (Z_{k+1} - \Psi_{k,k-1} Z_k - H_k^* \hat{X}_k). \quad (27)$$

The expression of new Kalman gain is

$$\bar{K}_{k+1} = (\phi_{k+1,k} P_k H_k^{*T} + \Gamma_k S_k) (H_k^* P_k H_k^{*T} + R_k^*)^{-1}. \quad (28)$$

The process noise covariance matrix is

$$P_{k+1}^* = \phi_{k+1,k} P_k^* \phi_{k+1,k}^T + \Gamma_k Q_k \Gamma_k^T - \bar{K}_{k+1} (H_k^* P_k^* \phi_{k+1,k}^T + S_k^T \Gamma_k^T). \quad (29)$$

The formula of EKF algorithm subject to colored measurement noise is given by Eq. (26)-Eq. (29).

IV. PAAM Control Loop Design

In a LISA-type mission, unlike the EKF considered before for clock synchronization purposes in the pre-TDI data post-processing^[10], the AEKF for PAAM will be carried out on orbit. In our design of the PAAM control, the FPGA control chip receives the feedback signal from the four-quadrant detector demodulated by the phasemeter and the capacitance sensors of PAAM. It combines the information of the SC orbit integrator for feedforward control. Fig 4 shows the block diagram design of the control system of the PAAM. In this control system, a theoretical model is established by AEKF and SC orbital integrator to control the PAAM. The output value controlled by the PID is weighted with the system noise as the state input to AEKF, and the measurement noise is added to simulate the actual situation on the SC. The whole control loop is closed-loop controlled by a phasemeter demodulated four-quadrant detector and capacitance sensors. Taking into account the creep and hysteresis of piezoelectric ceramics in the PAAM, nonlinear compensation, and notch filters are added to the control loop to improve the stability of the whole control loop.

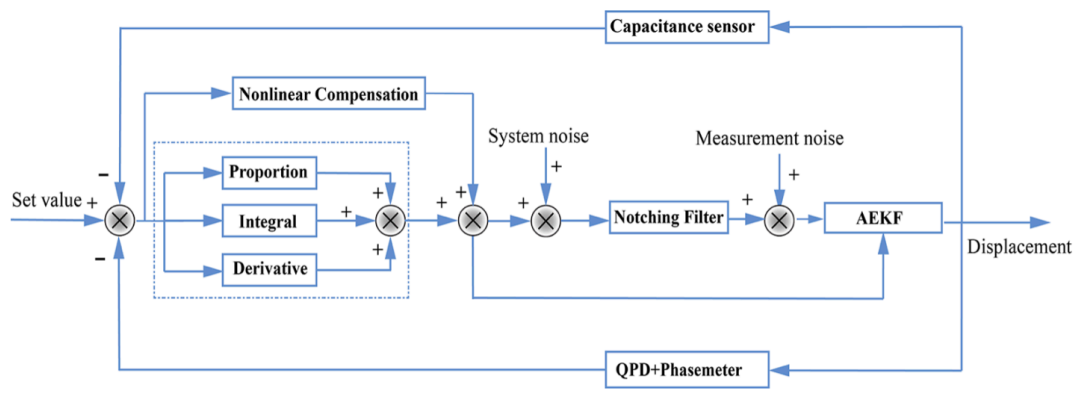


Figure 4. PAAM control framework.

The sampling frequency is chosen to be one per day, for the reason that the PAA varies slowly with the orbit. Further, in every manoeuvre of the PAAM, the piston noise couples with spacecraft attitude jitter and possibly other noise sources and generate position noise for gravitational wave measurement. A low sampling frequency will minimise the disturbance in the laser interferometry measurement.

Unlike the EKF considered before for clock synchronization purposes in the pre-TDI data post-processing^[11], the AEKF for PAAM will be carried out on orbit, and input of measurement data from the precision orbit determination of SCs is required. As the distance between the Earth and the triangle constellation is very similar to that between Mars and the Earth, the experience for the precision orbit determination of the Martian mission Tianwen I^[12] will serve as a useful reference guide. As the sampling frequency is one data per day, a straightforward way will be for the ground tracking station to upload the orbit data once per day. The delay for communication between the ground tracking station and SC (around half an hour) will be negligible due to the adiabatic, very slow change in the orbit of the triangle constellation. However, from the viewpoint of autonomous navigation and from the experience of the Tianwen I mission, it is feasible to use orbit prediction data for a month in the measurement model of the AEKF, provided the required precision in orbit determination on the position and velocity of SC orbit are respectively within the margins of 20km and 2cm/s^[13]. We can also update the orbit determination error by ground tracking during data transmission between the spacecraft and the ground station.

V. Adaptive extended Kalman Filter Model for PAAM

First, we define a 18-dimensional column state vector, which includes the position and velocity information of three SCs.

$$\mathbf{X}_k = [X_1, Y_1, Z_1, V_{X1}, V_{Y1}, V_{Z1}, X_2, Y_2, Z_2, V_{X2}, V_{Y2}, V_{Z2}, X_3, Y_3, Z_3, V_{X3}, V_{Y3}, V_{Z3}]^T. \quad (30)$$

The dynamics of a single SC is described by Keplerian equation for planetary motion given by

$$\ddot{\vec{X}}_k = \sum_{planet} GM_{planet} \frac{\vec{X}_k - \mathbf{R}_{planet}}{|\vec{X}_k - \mathbf{R}_{planet}|^3}, \quad (31)$$

Where \vec{X}_k is the position of one SC, M_{planet} , \mathbf{R}_{planet} are the mass and the coordinates of the i th celestial body (the Sun and the planets) in the solar system, $\vec{X}_k - \mathbf{R}_{planet}$ is a vector pointing from that SC to the i th celestial body. In designing the orbit used in our study, we considered only the gravitational forces given by the Sun and the major planets of the solar system when constructing the equations of motion for SC. The major planets include Mercury, Venus, Earth+Moon, Mars, Jupiter, Saturn, Uranus, and Neptune^[4]. The dynamic equation can be written in a different form.

$$\frac{d}{dt} \begin{bmatrix} \vec{X}_k \\ \vec{v}_k \end{bmatrix} = f(\vec{X}_k, \vec{v}_k) = \begin{bmatrix} \vec{v}_k \\ \sum_{planet} GM_{planet} \frac{\vec{X}_k - \mathbf{R}_{planet}}{|\vec{X}_k - \mathbf{R}_{planet}|^3} \end{bmatrix}. \quad (32)$$

We define $\alpha = (\vec{X}_k, \vec{v}_k)^T$, then we have

$$\phi = \frac{\partial f}{\partial \alpha} = \begin{bmatrix} \mathbb{O}_3 & \mathbb{I}_3 \\ A & \mathbb{O} \end{bmatrix}. \quad (33)$$

Here, \mathbb{O}_3 is the 3×3 zero matrix, \mathbb{I}_3 is the 3×3 identity matrix, and the expression of the 3×3 matrix A is given as:

$$A = - \sum_{planet} \frac{GM_{planet}}{|\vec{X}_k - \mathbf{R}_{planet}|^3} \mathbf{I}_3 + \sum_{planet} \frac{3GM_{planet}}{|\vec{X}_k - \mathbf{R}_{planet}|^5} (\vec{X}_k - \mathbf{R}_{planet}) (\vec{X}_k - \mathbf{R}_{planet})^T. \quad (34)$$

For the entire system, the dynamic matrix $\phi = \frac{\partial f}{\partial x}$ is 18×18 . We omit its explicit expression here, as it can be obtained in a straightforward way from the above formulae. In our work that follows, we simulate the PAA data of 3 years. Since the PAA changes very slowly with one year periodicity, we set the sampling frequency of the AEKF to 1 day. A longer time span up to a few days is also feasible. In the initial design process, we have considered the influence of SCs displacement, velocity, and acceleration on PAA, but in our subsequent simulation, we find that the relative acceleration of the SC is irrelevant to the PAA calculations.

Next, we shall present the two-dimensional measurement equation. The measurement equation which links up the positions and velocities of the three SCs and the in-plane and out-of-plane PAAs and may be written as

$$Z_k = h_k(X_k, v_k) = [\text{PAA}_{\text{out},12}, \text{PAA}_{\text{in},12}], \quad (35)$$

where $\text{PAA}_{\text{in},12}$ and $\text{PAA}_{\text{out},12}$ are respectively the in-plane PAA and the out-of-plane PAA. v_k is the measurement noise. H_k is a 2×18 -dimensional observation matrix. We omit the explicit of the 36 components in H_k . The element $H_k[i, j]$ in the matrix H_k may be expressed as:

$$H_k[i, j] = \frac{\partial Z_k[i]}{\partial X_k[j]}. \quad (36)$$

As an example, the [1,1] and [2,1] components of H_k , with the step index k omitted, may be given as follows.

$$H[1, 1] = \frac{\partial \text{PAA}_{\text{out},12}}{\partial X_1} = \frac{e_{zx} |\vec{R}_{r,12}|^2 - (\vec{e}_{z,12} \cdot \vec{R}_{r,12}) (x_{12} - V_{x12} \Delta t)}{|\vec{R}_{r,12}|^3}. \quad (37)$$

$\vec{e}_{z,12} \cdot \vec{R}_{r,12}$ is given in Eq. (20).

$$H[2, 1] = \frac{\partial \text{PAA}_{\text{in},12}}{\partial X_1} = \frac{\frac{\partial (\vec{R}_{r,12} \times \vec{e}_{z,12}) \cdot \vec{e}_{x,12}}{\partial X_1} - 2x_{12} \left((\vec{R}_{r,12} \times \vec{e}_{z,12}) \cdot \vec{e}_{x,12} \right)}{|\vec{R}_{r,12}| |\vec{R}_{t,12}|}.$$

with

$$\begin{aligned} & \frac{\partial \vec{R}_{r,12} \times \vec{e}_{z,12} \cdot \vec{e}_{x,12}}{\partial X_1} \\ &= (y_{12} - V_{y12} \Delta t) e_{zz} - (z_{12} - V_{z12} \Delta t) e_{zy} \\ & - e_{zz} (y_{12} + V_{y12} \Delta t) + e_{zy} (z_{12} + V_{z12} \Delta t), \end{aligned} \quad (38)$$

with $\vec{R}_{r,12} \times \vec{e}_{z,12} \cdot \vec{e}_{x,12}$ being given in Eq. (18).

In standard practice, the coefficient transfer matrix $\Psi_{k,k-1}$ of colored measurement noise is determined by the ARMA model. In the present context, the definition of $\Psi_{k,k-1}$ is relatively simple and can be considered as a special case of the ARMA model in which the autoregressive parameter is 1, and the moving average parameter is 0^[14]. We have also tried to use more sophisticated ARMA model to estimate the value of the $\Psi_{k,k-1}$ matrix, but the results are not as good as the methods used here. As shown in Eq. (21), we only consider the colored noise component in the measurement noise and did not include white noise. Therefore, the ξ_k term can be directly ignored. As shown in Eq. (39), we approximately take the ratio of the measurement noise amplitudes at the previous moment and the current moment as input

to the coefficient transfer matrix $\Psi_{k,k-1}$ of the colored measurement noise. The simple choice here is likely due to a very slow variation of the colored measurement noise in the time domain at an annual level. This colored measurement noise is a linear superposition of all colored noise, which we will discuss in detail in a moment.

$$\Psi_{k,k-1} = v_k/v_{k-1}. \quad (39)$$

In a standard adaptive Kalman filter, the size of the Q_k and R_k matrix is automatically adjusted by observing the prediction error and its mean square error matrix and introducing the fading factor to obtain a good estimation state^[15]. The AEKF designed in this paper is slightly different from the traditional AEKF. In the AEKF designed by us, the covariance matrix of measurement noise R_k is updated in real-time according to the magnitude of measurement noise, while the covariance matrix of system noise Q_k is updated every month or so, based on the accuracy of orbit prediction. It can also be updated by ground tracking during data transmission between the spacecraft and the ground station.

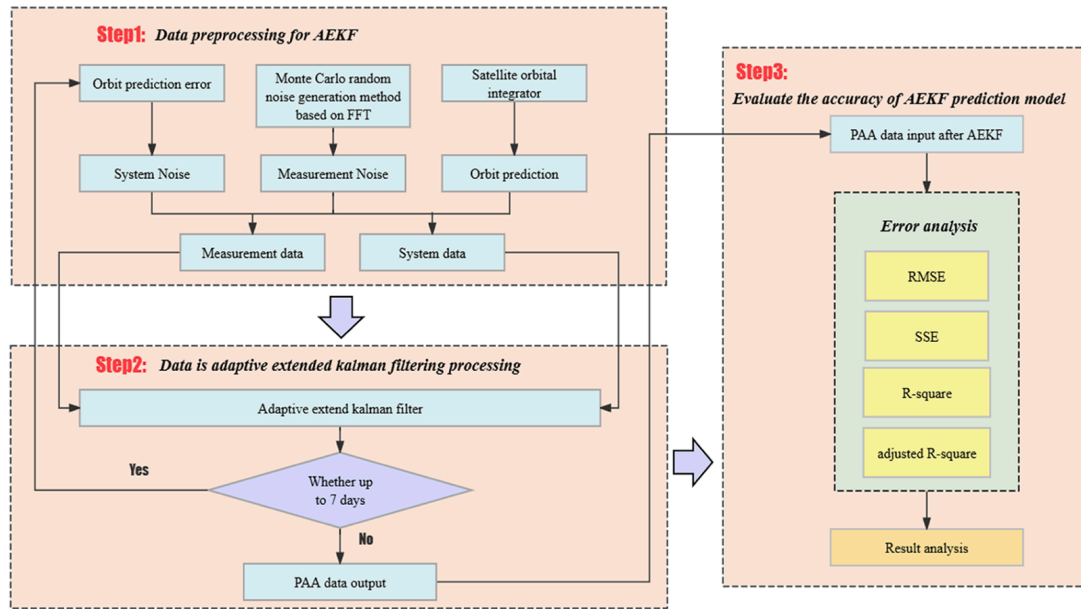


Figure 5. PAA calculation flow chart.

In this study, the flowchart for PAA adjustment computation is illustrated in Fig. 5. During the first step of data preprocessing, we rely on orbit prediction to acquire the SC's position and velocity information. The error in orbit prediction within this system is linearly superimposed onto the orbit prediction data as system noise to form the system data. The orbit prediction data, linearly superimposed with noise

generated by the FFT-based Monte Carlo random noise generation method, constitutes the measurement data input into the AEKF. The system data and measurement data are generated using different orbital prediction data, each based on different points of the orbital determination error as input. At the same time, the orbital determination error can also be obtained without orbital prediction. During data transmission between the spacecraft and the ground station, ground tracking can also be used to update it. In the second step, during the AEKF process, the orbit prediction information needs to be updated every month. In the third step, we conduct an error analysis on the data filtered by AEKF, using four independent methods: SSE (Sum of Squared Errors), RMSE (Root Mean Squared Error), R-square, and adjusted R-square for error fitting. Finally, the results are analyzed and discussed.

VI. System Noise Model

To work out a system model for AEKF, consider

$$\begin{cases} \delta X = [\delta x, \delta y, \delta z]^T, \\ \delta V = [\delta V_x, \delta V_y, \delta V_z]^T. \end{cases} \quad (40)$$

where δX and δV are the errors in respectively the position and velocity in the orbit prediction. We take the SC's position and velocity data generated by the orbit integrator as input into the AEKF while incorporating the orbit prediction error in the form of system noise. Accordingly, we express the SC position coordinates $[X_i + \delta x, Y_i + \delta y, Z_i + \delta z]^T$ and velocity coordinates $[V_{Xi} + \delta V_x, V_{Yi} + \delta V_y, V_{Zi} + \delta V_z]^T$, Eq. (1) - Eq. (8) are then employed to calculate the PAA with orbital prediction errors taken into account. The position coordinates $[X_i, Y_i, Z_i]^T$ and velocity coordinates $[V_{Xi}, V_{Yi}, V_{Zi}]^T$ of the SC, free of orbital prediction errors, will be used to compute the true value of PAA by substituting them into Eq. (1)-(8). The difference between these two values represents the PAA error generated by the orbital prediction. This error is input as the source of system noise for the AEKF. We then transform this orbit prediction error into both in-plane and out-of-plane PAA errors, resulting in an error margin of approximately 0.2 nrad. The system noise is linearly superimposed onto the genuine PAA value provided by the orbital integrator in the form of white noise. Additionally, the covariance matrix Q_k is configured in accordance with the system noise.

VII. Measurement Noise Model

This section primarily elaborates on the PAA noise model, serving as the foundation for quantifying measurement noise in our subsequent simulations. During the simulation process, position and velocity

of SCs are generated by an the orbit integrator to mimic orbit prediction. We consider this to be the true value and linearly superimpose it with the measurement noise data, which serves as the input of the measurement value for AEKF. To better simulate the actual conditions on orbit, we adopt an FFT-based Monte Carlo method to generate random time-domain noise signals with specified PSD. Specifically, the colored noise generated by this method is produced using the LISA noise PSD in the time domain with the help of the LTPDA toolkit^[16]. At the same time, the covariance matrix R_k , which characterizes the measurement noise within the AEKF, is dynamically computed from the generated noise and updated in real-time^[17] as

$$R_k = \text{cov}[v_k, v_k]. \quad (41)$$

The noise model accounts for various sources, and we add a total of $10 \times 10^{-12} \frac{m}{\sqrt{Hz}}$ measurement noise, taking into account mainly piston noise of PAAM, directional jitter noise, SC attitude jitter noise, readout noise among others. In AEKF, since the measurement noise is much larger than the system noise, the size of its prediction error mainly depends on the size of the system noise. Therefore, increasing the measurement noise does not significantly affect the prediction results. Then, we use the LTPDA toolbox to generate time-domain noise based on the noise power spectral density function. The sum of the measurement noise can be expressed as Eq. (42), and f is the frequency.

$$\tilde{x}_{\text{noise}}(f) = 10 \times 10^{-12} \sqrt{1 + \left(\frac{2.8\text{mHz}}{f} \right)^4} \frac{m}{\sqrt{Hz}}. \quad (42)$$

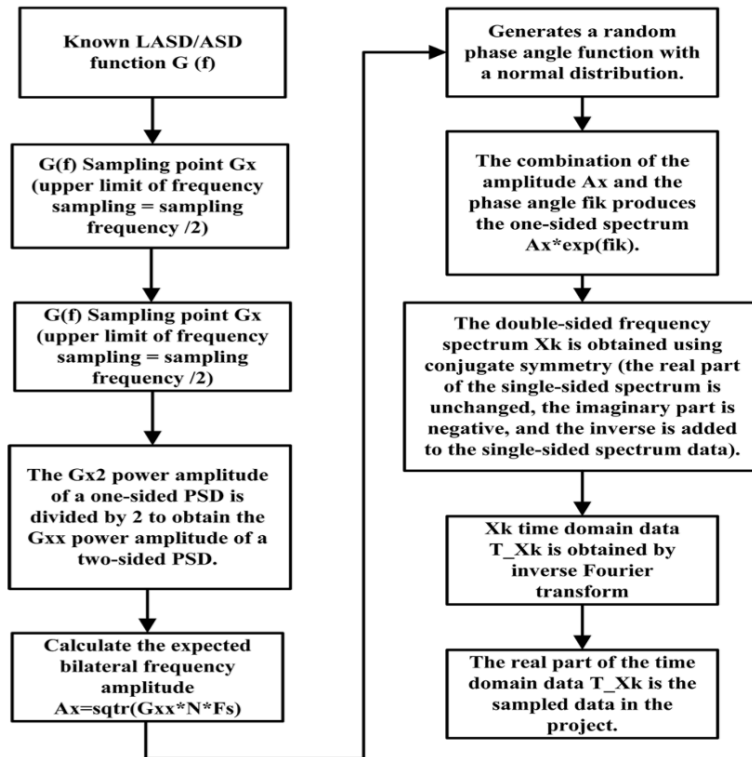


Figure 6. Flow chart of time domain noise acquisition.

The distribution of noise in the time domain is obtained by backpropagating the noise expression in the frequency domain using the LTPDA toolbox in with the flowchart shown in Fig. 6^[16]. Fig. 7 is the PSD curve of noise. The total displacement noise PSD is a linear superposition of a number of individual noise PSDs.

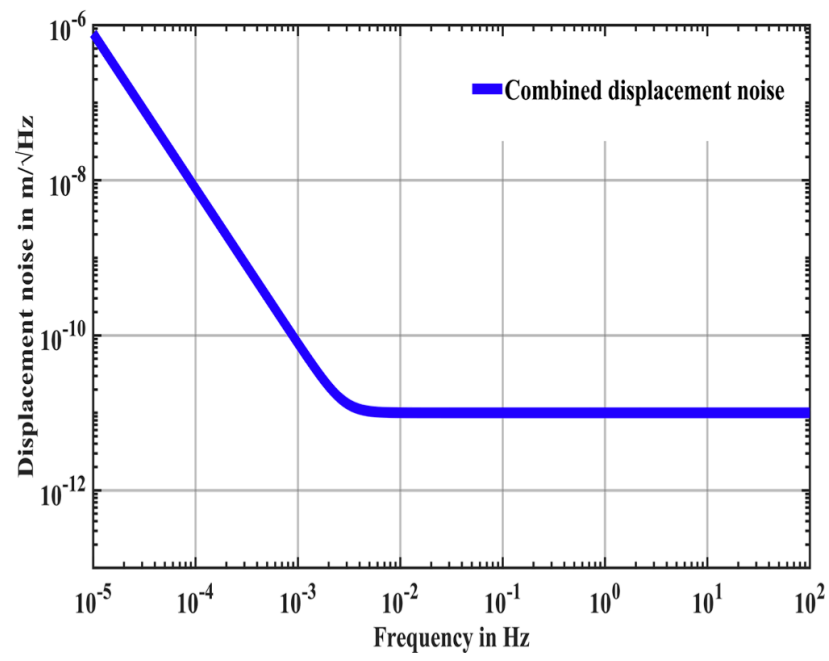


Figure 7. PAA noise model.

VIII. Simulation results.

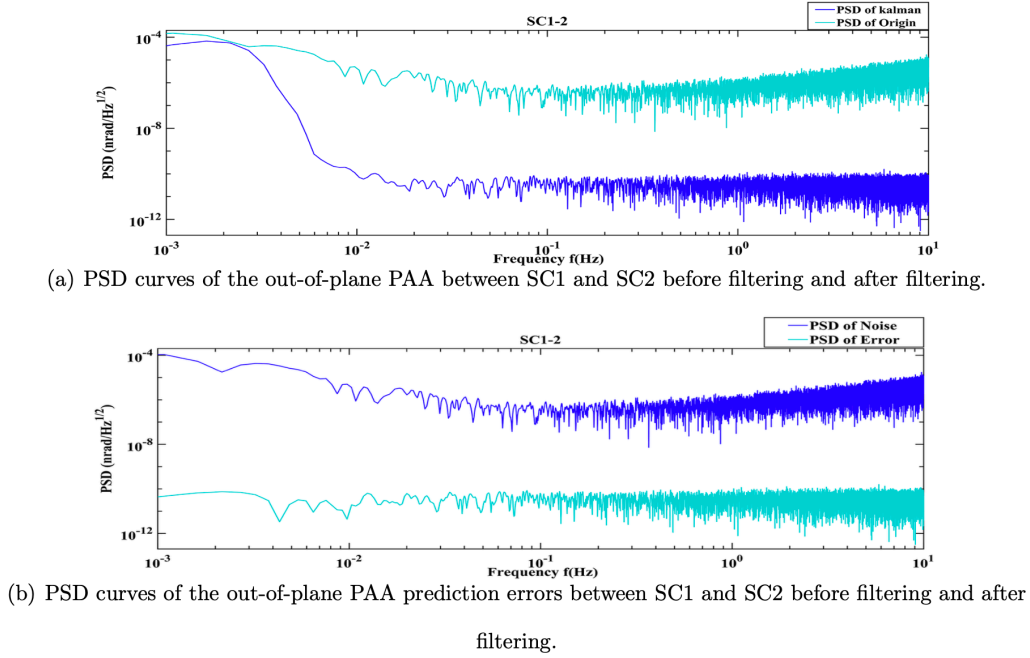
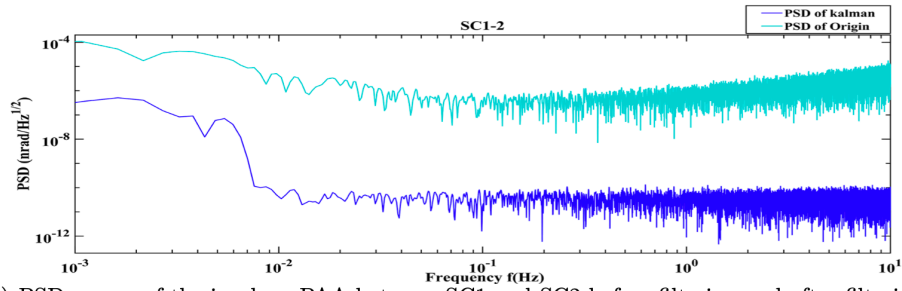
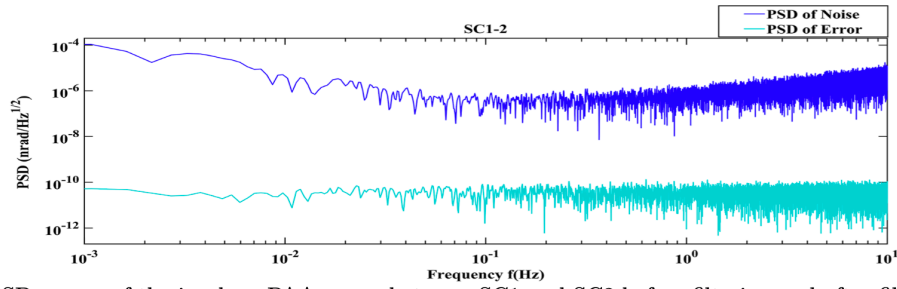


Figure 8. PSD curves of the out-of-plane PAA between SC1 and SC2.

Fig. 8(a) is the PSD curves of the out-of-plane PAA between SC1 and SC2 before filtering and after filtering. Fig. 8(b) is the PSD curves of the out-of-plane PAA errors between SC1 and SC2 before filtering and after filtering. Both figures show that the AEKF effectively filters high-frequency noise signals and low-frequency noise between 1 mHz and 10 Hz. The filtering effect of the AEKF in the high-frequency band is better than that at low frequency. In the band from 1 mHz to 0.01 Hz, the PSD of the out-of-plane PAA before filtering SC1 to SC2 is about $1.51 \times 10^{-4} \text{rad}/\sqrt{\text{Hz}}$, and it is reduced to about $4.69 \times 10^{-5} \text{rad}/\sqrt{\text{Hz}}$ after filtering. In the band from 1 mHz to 0.01 Hz, the PDS of the out-of-plane PAA before filtering is about $3.76 \times 10^{-6} \text{rad}/\sqrt{\text{Hz}}$, and it is reduced to about $5.88 \times 10^{-11} \text{rad}/\sqrt{\text{Hz}}$ after filtering. In the frequency window 1 Hz-10 Hz, The AEKF's noise PSD rejection ratio is about -3.9 dB near 1mHz, -48 dB near 0.01Hz, and close to -39 dB at 0.01Hz-10Hz.



(a) PSD curves of the in-plane PAA between SC1 and SC2 before filtering and after filtering.



(b) PSD curves of the in-plane PAA errors between SC1 and SC2 before filtering and after filtering.

Figure 9. PSD curves of the in-plane PAA between SC1 and SC2

Fig. 9(a) is the PSD curves of the in-plane PAA between SC1 and SC2 before filtering and after filtering. Fig. 9(b) is the PSD curves of the in-plane PAA errors between SC1 and SC2 before filtering and after filtering. Both Figures show that the AEKF effectively filters high-frequency noise signals and low-frequency noise between 1mHz and 10 Hz. The filtering effect of the AKEF in the high-frequency band is better than that at low frequency. In the band from 1mHz to 0.01Hz, the PSD of the in-plane PAA before filtering is about $1.06 \times 10^{-4} \text{ rad}/\sqrt{\text{Hz}}$, and it is reduced to about $3.57 \times 10^{-7} \text{ rad}/\sqrt{\text{Hz}}$ after filtering. In the band from 0.01 Hz to 10 Hz, the PSD of the in-plane PAA before filtering is about $3.76 \times 10^{-6} \text{ rad}/\sqrt{\text{Hz}}$, and it is reduced to about $3.48 \times 10^{-11} \text{ rad}/\sqrt{\text{Hz}}$ after filtering. The noise PSD rejection ratio of the AEKF is about -24.5dB near 1 mHz, -50.4dB near 0.01Hz, and close to -42dB at 0.01Hz-10Hz.

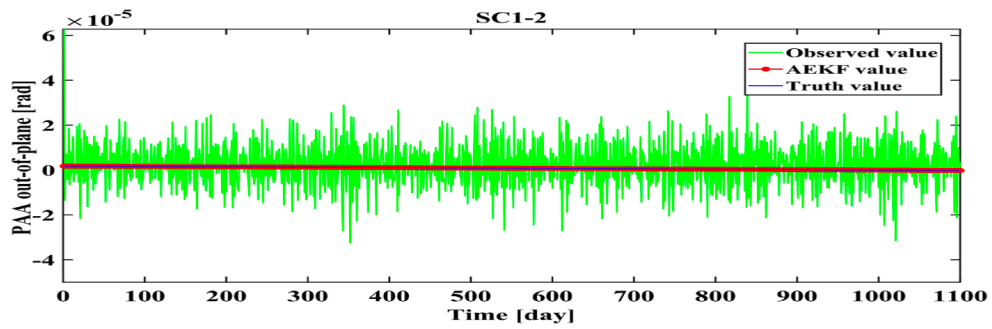


Figure 10. Out-of-Plane PAA between SC1 and SC2 before filtering and after filtering.

Fig. 10 shows the time domain noise curve of the out-of-plane PAA between SC1 and SC2 before filtering and the curve after Kalman filtering. This result reflects the time domain performance of the AEKF. The results show that the AEKF is efficient in noise suppression.

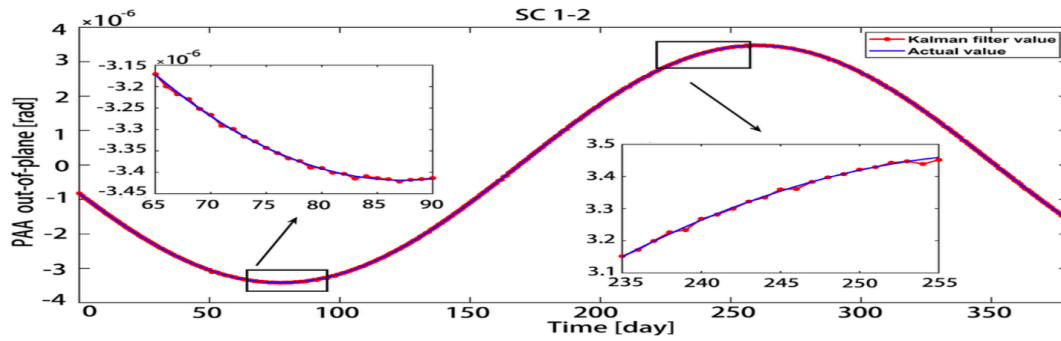


Figure 11. Out-of-plane PAA between SC1 and SC2 after filtering.

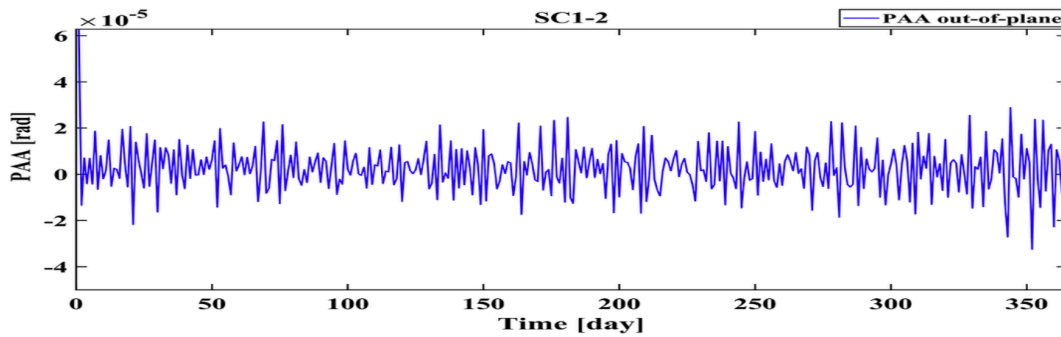


Figure 12. Prediction error of the out-of-plane PAA between SC1 and SC2.

Fig. 11 displays the AEKF result and the real values of the out-of-plane PAA between SC1 and SC2 variation in one year. Fig. 12 shows the prediction error of the out-of-plane PAA between SC1 and SC2 after Kalman filtering in the time domain. During 100–180 days and 300–360 days, their relative motion is uniform, and the Kalman filtered out-of-plane PAA closely matches the actual situation. At this time, the noise before filtering is about $63 \mu\text{rad}$, and after Kalman filtering, it reaches about 0.84 nrad . However, within 50–100 days and 180–300 days, there is a significant variation in the out-of-plane PAA. Consequently, the filter error during these periods is relatively large, about 0.95 nrad . This is mainly due to the large variation of relative velocity motion between two SCs.

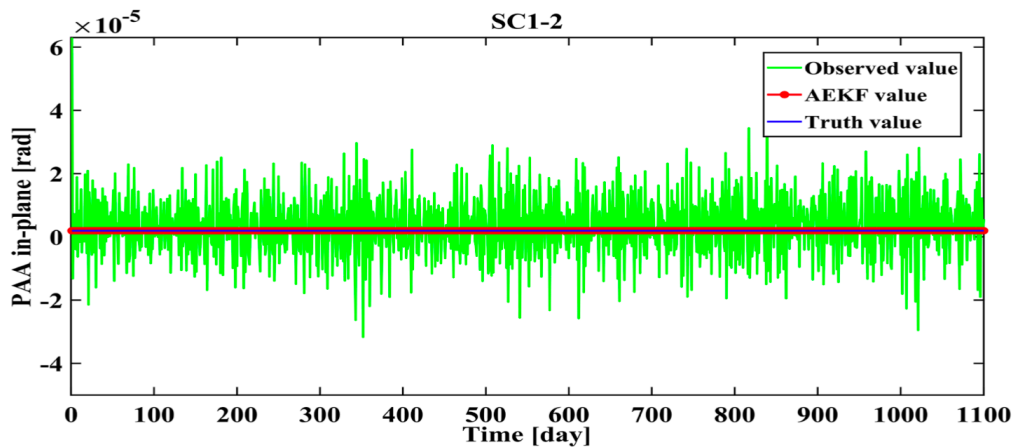


Figure 13. In-plane PAA between SC1 and SC2 before filtering and after filtering .

Fig. 13 displays the time domain noise curve of the in-plane PAA between SC1 and SC2 before filtering and after filtering. The results in the time domain reflect the noise reduction effect of the in-plane PAA under the AEKF. Compared with the out-of-plane PAA, the variation range of the in-plane PAA is reduced and the variation under the action of noise is evident. The in-plane PAA noise in the time domain shows a decreasing trend in the range of 50–100 days and an increasing trend in the range of 100–200 days.

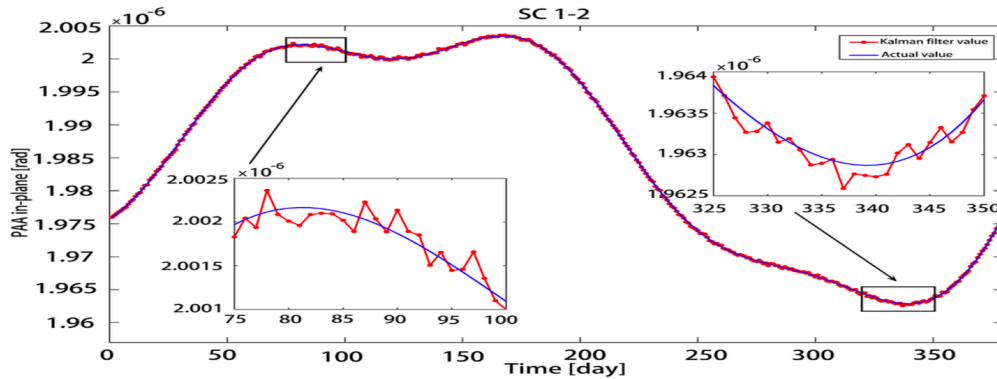


Figure 14. In-plane PAA between SC1 and SC2 after filtering.

Fig. 14 shows the AEKF result and the real values of the in-plane PAA between SC1 and SC2 variation in one year. Fig. 15 shows the prediction error of the in-plane PAA between SC1 and SC2 after Kalman filtering in the time domain. Compared with the out-of-plane PAA, the error variation of the in-plane PAA is more evident after Kalman filtering. Comparing the error before and after filtering, it may be seen that the AEKF algorithm can effectively suppress the in-plane PAA noise. The noise before filtering is about $63 \mu\text{rad}$, while the pointing error after AEKF filtering is less than 1 nrad .

VIII.1. Summary of the main results.

Parameters	SC12	SC13	SC21	SC23	SC31	SC32
Observed PAA out/(rad)	6.987E-5	6.883E-5	6.916E-5	6.884E-5	6.812E-5	6.912E-5
Observed PAA in/(rad)	6.584E-5	6.413E-5	6.622E-5	6.418E-5	6.602E-5	6.512E-5
AEKF PAA out/(rad)	6.899E-6	6.905E-6	6.899E-6	6.893E-6	6.905E-6	6.892E-6
AEKF PAA in/(rad)	3.743E-8	3.967E-8	3.750E-8	4.112E-8	4.65E-8	4.531E-8
Ideal PAA out/(rad)	6.899E-6	6.905E-6	6.899E-6	6.892E-6	6.905E-6	6.892E-6
Ideal PAA in/(rad)	3.708E-8	6.633E-8	3.708E-8	4.483E-8	6.633E-8	4.483E-8

Table I. Dynamic range of the PAA.

We will give a recap of the main results at the end of this section. The dynamic range of PAA is dependent on error in the precision orbit determination of SCs. When the position determination error of the SC is 20km and the velocity error is 2cm/s, the dynamic range of the out-of-plane PAA and the in-plane PAA is about 63 μrad . With AEKF inserted into the control loop, the dynamic range of the out-of-plane PAA is approximately reduced to 6.9 μrad , and the dynamic range of the in-plane PAA is approximately reduced to 40 nrad. The result shows that the dynamic range of the PAA can be effectively reduced by AEKF even in the presence of error in precision orbit determination.

Based on the analysis of the filtering results in the frequency domain, the error of the in-plane PAA and the out-of-plane PAA decreases significantly at high-frequency ends. In the band from 0.01 Hz to 10 Hz, the filtering error signal is less than 1 nrad/ $\sqrt{\text{Hz}}$. The filtering effect of AEKF at low frequency is not as good as that at high frequency.

Parameters	SC12	SC13	SC21	SC23	SC31	SC32
PAA-OUT/(nrad)	0.957	0.857	0.940	0.941	0.882	0.852
PAA-IN(nrad)	0.846	0.833	0.845	0.920	0.972	0.814

Table II. Prediction error of PAA in-plane and out-of-plane.

In our simulation, orbital dynamics and the update of the SC's state of motion are input into the iterations of the AEKF. Table II summarizes the results of the maximum prediction errors before and after filtering the in-plane PAA and the out-of-plane PAA between the two SCs. The results in Table I show that the AEKF can effectively suppress the pointing noise of the PAA.

Parameters	SC12	SC13	SC21	SC23	SC31	SC32
SSE	4.0985E-29	7.06114E-29	1.5231E-28	7.4431E-29	5.5912E-29	8.10921E-30
RMSE	1.7019E-16	2.23388E-16	3.28085E-16	2.2935E-16	1.98781E-16	7.57027E-17
R-square	1	1	1	1	1	1
adjusted R-square	1	1	1	1	1	1

Table III. Fitting result.

In our simulation, we conduct a fitting precision analysis on the discrete PAA values after filtering through the AEKF. The fitting accuracy can be evaluated using SSE, R-square, adjusted R-square, and Root Mean Squared Error (RMSE). The fitting results are shown in Table III. Both R-square and adjusted R-square are close to 1, SSE and RMSE are close to 0, indicating a good fit and that the fitting accuracy meets our requirements.

IX. Concluding remarks

In the present work, by exploiting the simple orbital structure of SC motion in the triangular constellation, the feasibility of incorporating an AEKF in the PAAM is considered. The simulation results show that the dynamic range of the PAAM may be drastically reduced. This will cut down on the TTL coupling noise and the position noise budget allocated to the instrument. At the same time, the dynamic range of the fine pointing control is also reduced and leaves room for the improvement of accuracy for the fine pointing control. The position noise budget allocated to the pointing stability control may be reduced as a whole.

Though our calculations look complicated as we try to spell out the details of the derivation, the actual implementation of the Kalman filter is very simple. From our flight experience with the adaptive AEKF for star sensors and, again, due to the simplicity of the orbital dynamics of the three SCs, we expect the AEKF for PAAM will only consume a little computational resource on board. In our next step, we are setting up a desktop experiment to verify the AEKF constructed here in a hardware setting. Further, we are also considering the employment of the Kalman-filtered PAAM to improve the capture time and efficiency in the ATP phase. We hope to report further progress in this direction soon.

X. Appendices

In the main text, simulation results are presented only for a single arm out of the three arms in the triangular constellation of SCs, as simulation results are almost identical for the the three arms. In this appendix, for completeness, simulation results for all three arms are presented.

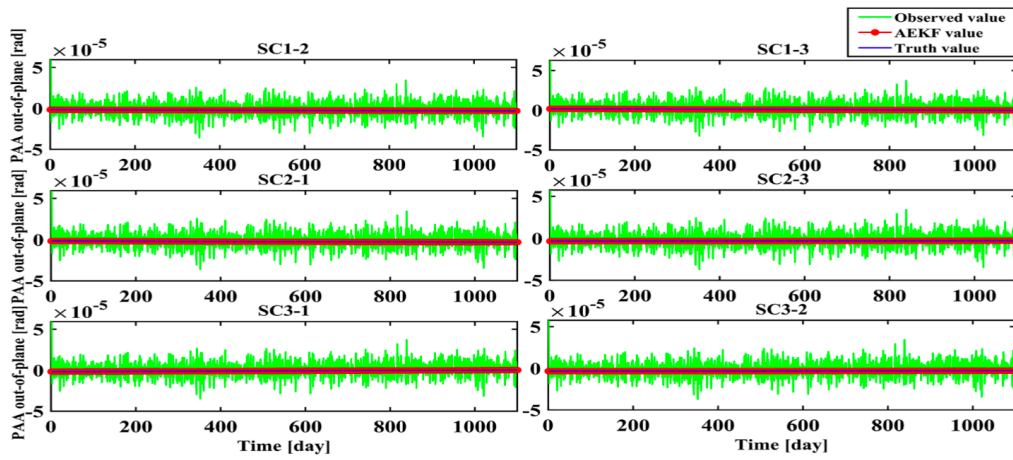


Figure 16. Out-of-plane PAA after filtering.

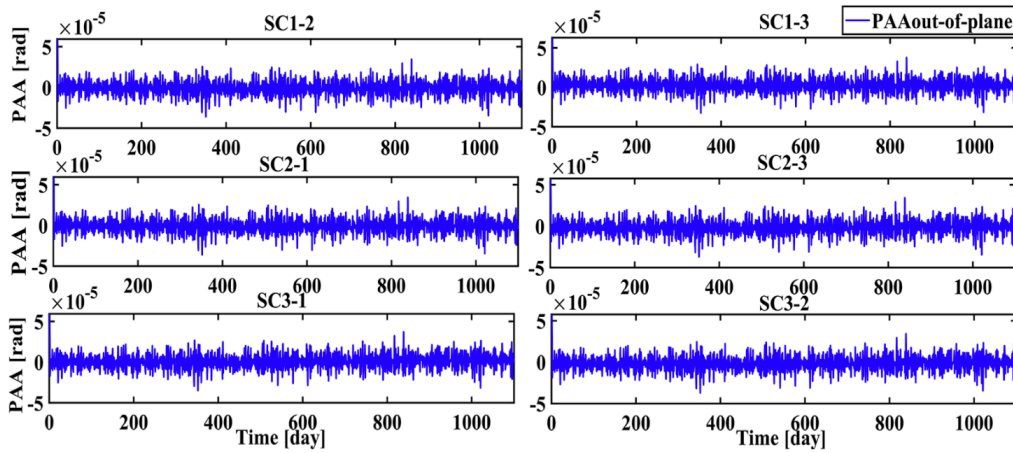


Figure 17. Prediction error of the out-of-plane PAA.

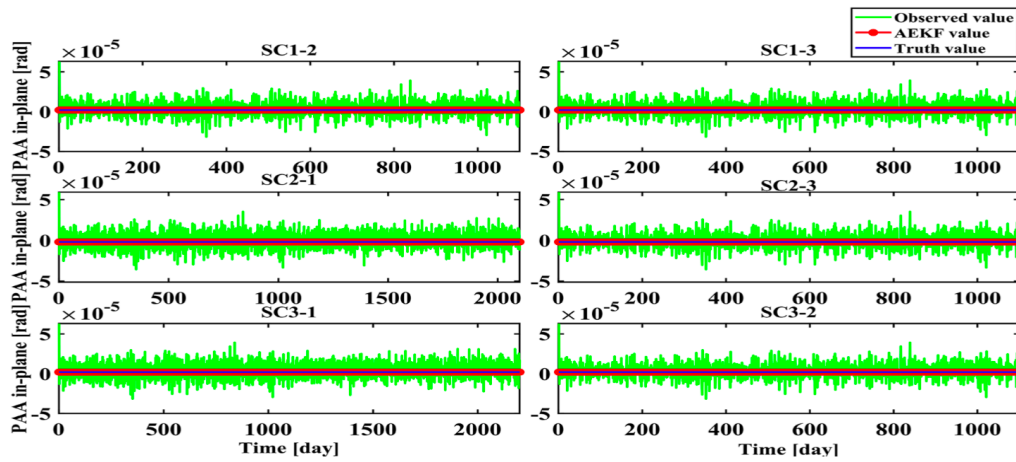


Figure 18. In-plane PAA after filtering.

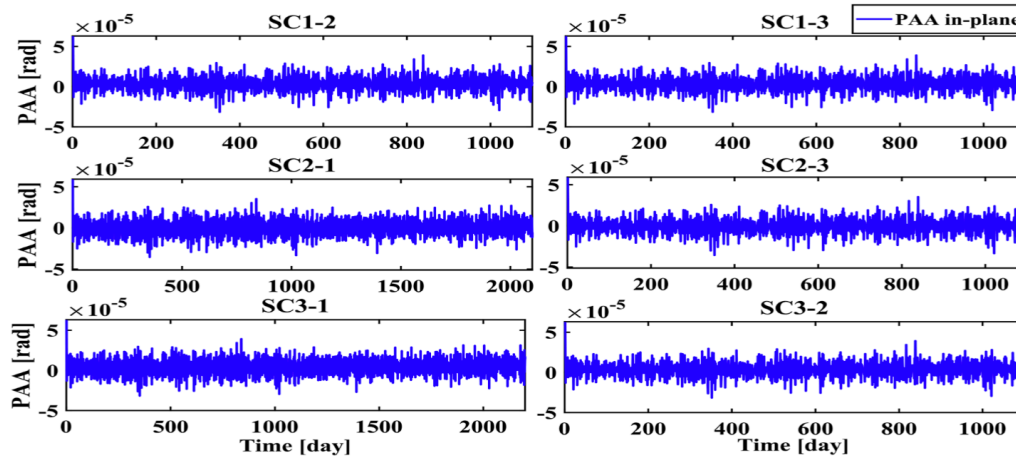


Figure 19. Prediction error of the in-plane PAA.

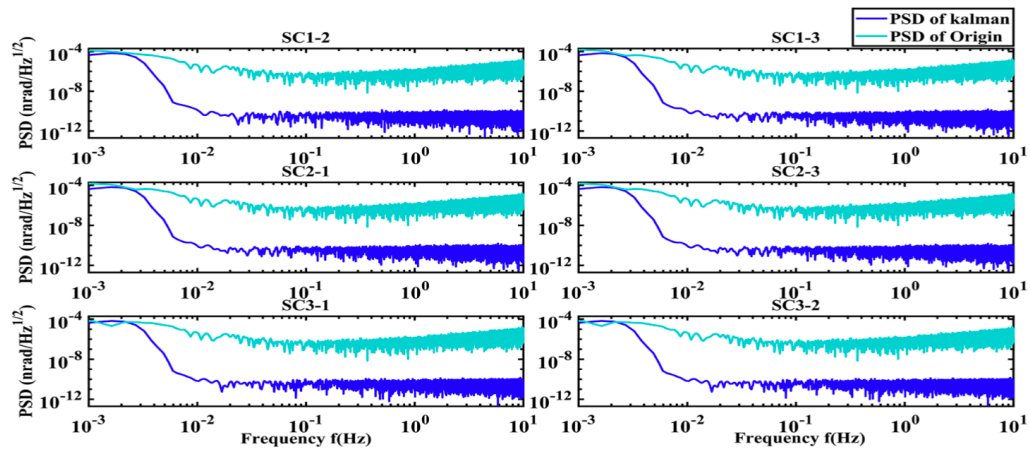


Figure 20. Out-of-plane PAA PSD curve before and after filtering.

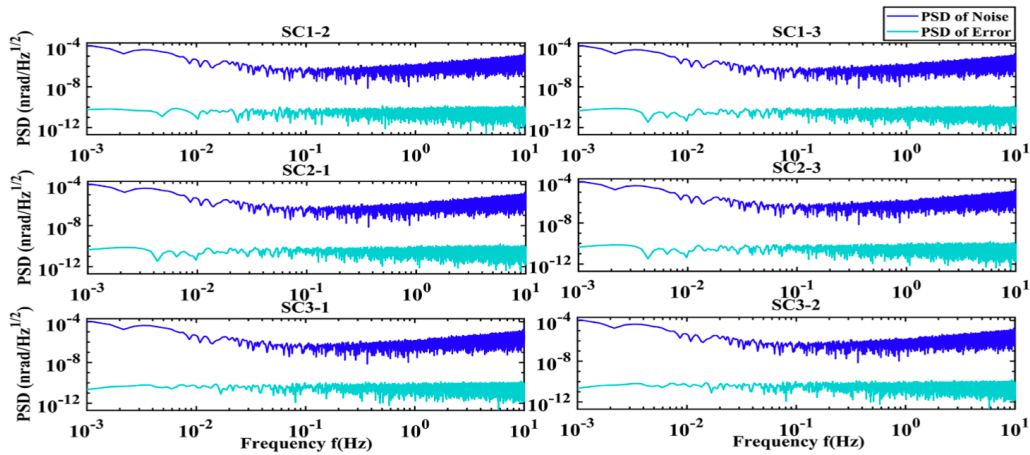


Figure 21. PSD curve of the out-of-plane PAA error before and after filtering.

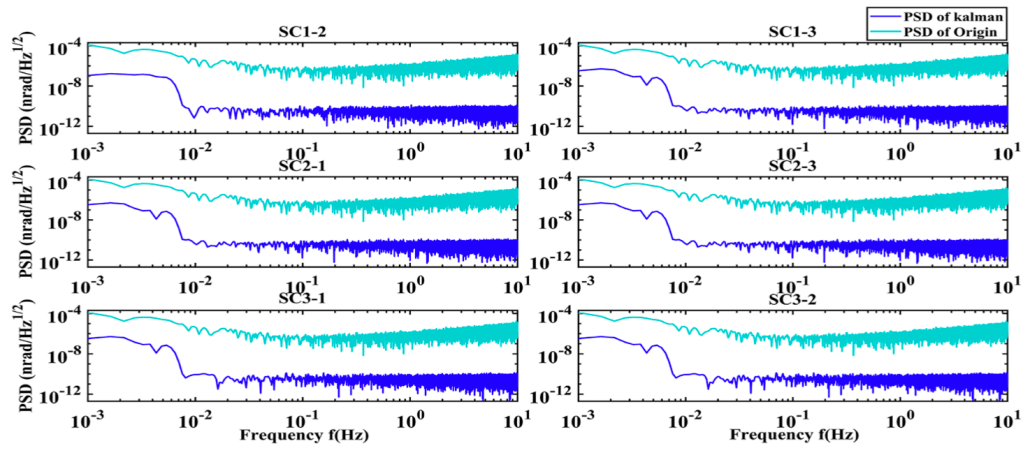


Figure 22. In-plane PAA PSD curve before and after filtering.

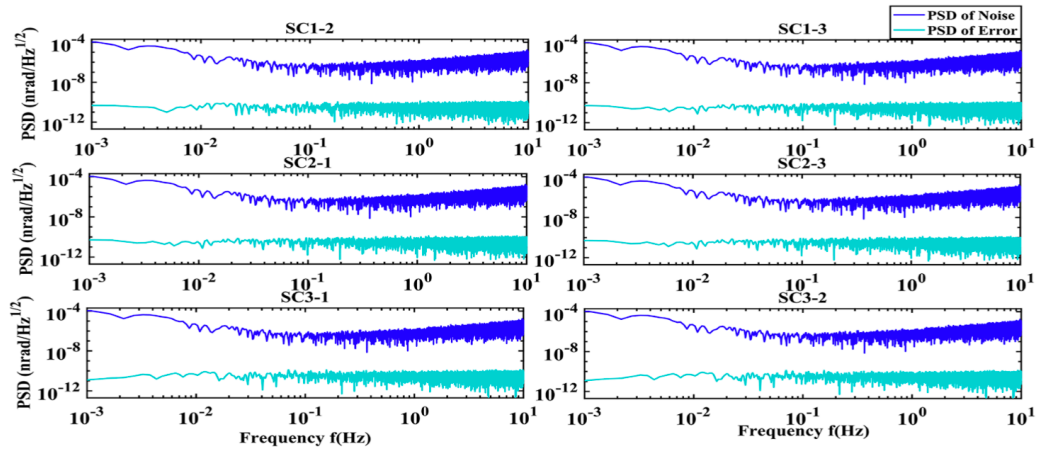


Figure 23. PSD curve of the in-plane PAA error before and after filtering.

Acknowledgements

This work is supported by the National Key R&D Program of China (2022YFC2203701).

References

1. [△]Luo Z, Guo Z, Jin G, Wu Y, Hu W (2020). "A brief analysis to Taiji: Science and technology". *Results in Physics* s. 16: 102918.

2. ^aDanzmann K, LISA Study Team, et al. LISA: laser interferometer space antenna for gravitational wave measurements. *Classical and Quantum Gravity*. **13** (11A): A247 (1996).
3. ^aLuo J, Chen L-S, Duan H-Z, Gong Y-G, Hu S, Ji J, Liu Q, Mei J, Milyukov V, Sazhin M, et al. TianQin: a space-borne gravitational wave detector. *Classical and Quantum Gravity*. **33** (3): 035010 (2016).
4. ^{a, b, c}Han X, Peng X, Tang W, Yang Z, Ma X, Gao C, Qiang L-e, Zhang Y, Zhao M, Zhang J, Liu B (2022). "Effect of celestial body gravity on Taiji mission range and range acceleration noise". *Physical Review D*. **106** (10): 102005.
5. ^aHouba N, Delchambre S, Ziegler T, Hechenblaikner G, Fichter W (2022). LISA Point-Ahead Angle Control for Optimal Tilt-to-Length Noise Estimation. *arXiv preprint arXiv:2208.11033*. Available from: <https://arxiv.org/abs/2208.11033>.
6. ^{a, b}Simon D (2006). *Optimal state estimation: Kalman, H_∞ , and nonlinear approaches*. Hoboken, NJ: John Wiley and Sons, Jg. **10**: 0470045345.
7. ^aLjung L. Asymptotic behavior of the extended Kalman filter as a parameter estimator for linear systems. *IEEE Transactions on Automatic Control*. **24** (1): 36–50 (1979).
8. ^aXu Y, Shmaliy YS, Bi S, Chen X, Zhuang Y (2023). Extended Kalman/UFIR Filters for UWB-based Indoor Robot Localization under Time-Varying Colored Measurement Noise. *IEEE Internet of Things Journal*. (2023).
9. ^aChang G. "On kalman filter for linear system with colored measurement noise". *Journal of Geodesy*. **88** (12): 1163–1170 (2014).
10. ^aWang Y, Heinzel G, Danzmann K (2014). "First stage of LISA data processing: Clock synchronization and arm-length determination via a hybrid-extended Kalman filter". *Physical Review D*. **90** (6): 064016.
11. ^aWang Y, Heinzel G, Danzmann K (2015). "First stage of LISA data processing. II. Alternative filtering dynamic models for LISA". *Physical Review D*. **92** (4): 044037.
12. ^aYang P, Huang Y, Li P, Wang H, Fan M, Liu S, Shan Q, Qin S, Liu Q (2022). "Orbit determination of China's first mars probe Tianwen-1 during interplanetary cruise". *Advances in Space Research*. **69** (2): 1060–1071.
13. ^aLi Z, Zheng J (2021). Orbit determination for a space-based gravitational wave observatory. *Acta Astronautica*. **185**: 170–178.
14. ^aFattah S, Zhu W-P, Ahmad M (2011). "Identification of autoregressive moving average systems based on noise compensation in the correlation domain". *IET signal processing*. **5** (3): 292–305.
15. ^aMohamed A, Schwarz K (1999). "Adaptive Kalman filtering for INS/GPS". *Journal of geodesy*. **73**: 193–203.
16. ^{a, b}Hewitson M, Armano M, Benedetti M, Bogenstahl J, Bortoluzzi D, Bosetti P, Brandt N, Cavalleri A, Ciani G, Cristofolini I, et al. Data analysis for the LISA Technology Package. *Classical and Quantum Gravity*. **26**(9):

094003 (2009).

17. ^ΔKaba U, Temeltas H (2022). Generalized bias compensated pseudolinear Kalman filter for colored noisy bearings-only measurements. *Signal Processing*. **190**: 108331.

Declarations

Funding: This work is supported by the National Key R&D Program of China (2022YFC2203701).

Potential competing interests: No potential competing interests to declare.